Alma Mater Studiorum Università di Bologna
Archivio istituzionale della ricerca

Impact of carbon dioxide and nitrogen addition on the global structure of hydrogen flames

(Article begins on next page)

19 February 2025

Impact of carbon dioxide and nitrogen addition on the global structure of hydrogen flames

S. Eckart[1], G. Pio[2], T. Zirwes[3,4], F. Zhang[4], E. Salzano[2], H. Krause[1], H, Bockhorn[4]

Sven Eckart: sven.eckart@iwtt.tu-freiberg.de

[1]*Institute of Thermal Engineering, TU Bergakademie Freiberg, Freiberg, Germany*

[2]*Department of Civil, Chemical, Environmental and Materials Engineering, University of Bologna, Italy*

[3]*Steinbuch Centre for Computing, Karlsruhe Institute of Technology, Germany*

[4]*Engler-Bunte-Institute, Division of Combustion Technology, Karlsruhe Institute of Technology, Germany*

Abstract

Investigations into the combustion characteristics and flame structure of hydrogen/air flames with different dilutions of hydrogen with carbon dioxide have been carried out experimentally and numerically. The aim was to determine the variations of the flame shape for different carbon dioxide dilutions in the H_2-air mixtures. For this purpose, premixed flames at various compositions of hydrogen-carbon dioxide mixtures are investigated experimentally in a heat flux burner configuration at varying equivalence ratios from 0.5 to 1.1, fresh gas temperatures and under atmospheric conditions. Optical investigations are performed to detect the number of cellular structures on the flame front. Furthermore, the laminar burning velocity and the influence of carbon dioxide addition were examined numerically. A detailed kinetic mechanism was implemented for the identification of the most representative intermediates via a reaction path analysis, and the most influential species and reactions are identified through sensitivity analyses at conditions relevant to the studied application. Considering the nature of the adopted mechanism, the presence of CO_2 has the potential to shift the production/consumption rate of some hydrogen-containing radicals. Hence, numerical investigations employing an inert species having the same thermodynamic and transport properties as CO_2 (referred to as fictitious CO_2, FCO_2) were

30   compared and discussed in this work. To investigate the effect of CO_2 on the dynamics of the hydrogen

31   flames, one-dimensional and two-dimensional detailed simulations of the flame structure have been

32   carried out. The addition of CO_2 makes the flame more prone to thermo-diffusive instabilities through a

33   decrease in the mixture's thermal diffusivity. This results in a decrease of the Markstein number and an

34   enhanced formation of characteristic cellular structures on spherically expanding flames. Overall the

35   comparison between the experimental and numerical investigations reveals similar conclusions.

36

37   Keywords: hydrogen admixtures, flame structure, CO_2, cellular structures

38

39   **Introduction**

40   To reduce CO_2 emissions, fossil fuels, such as natural gas, have to be replaced in the gas supply

41   system by non-fossil energy carries, such as hydrogen produced preferably from renewable sources. In

42   this context, carbon oxides as by-products from hydrogen manufacturing are an increasingly important

43   issue in the utilization of lower grade hydrogen. Technologies needed for the industrial utilization of

44   hydrogen, e.g. safe transport and optimised combustion, are under rapid development or in the

45   prototype stadium. Numerous industrial thermo-processes could run on gaseous mixtures rich in H_2 and

46   CO_2, including hydrogen from biomass conversion, plastic waste treatment, thermal processes, steam

47   reforming, and gasification processes [1]. Undoubtedly, new technologies based on H_2 for providing of

48   energy (e.g., integrated gasification combined cycle or gas turbines) have been considerably improved

49   in the last decades for reduction of air pollution. Commonly, a large variety of processed materials or

50   operating conditions can be applied for these processes. For example, steam reforming and gasification

51   can implement different charges (e.g., methane, naphtha, or coal) and have several target products

52   (e.g., hydrogen, methanol, or ammonia), resulting in considerably different compositions of the product

53   stream from the reactor (see Table 1, adapted from [2,3]).

54   These product streams usually are treated via several conversion and separation processes aiming

55   at the reduction of impurities (e.g., sulphur-based species) and undesired by-products. Considering that

56   95 % of H_2 is produced via steam reforming worldwide [1], particular attention is paid to the conversion

57   of CO when H_2 is manufactured for providing of energy. In this case, shift reactors are commonly

58   integrated into the process to convert CO (Equation 1), with obvious implications on the H_2 to CO_2

59 volume ratio. Based on data reported in refs [1-4] for the ratio of H_2/CO for gasification processes, a

60 proper amount of steam must be provided.

61 $$H_2O + CO \leftrightharpoons CO_2 + H_2 \tag{1}$$
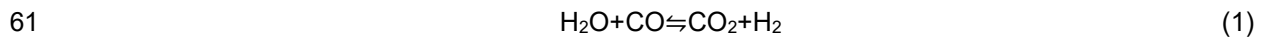
62

63 **Table 1** Typical composition of products gases from industrial processes delivering gaseous

64 mixtures rich in H_2 and CO_2. Adapted from [2,3]

Process	H_2	CO	CO_2	CH_4	H_2O	H_2/CO_2	C/H
SR (Methane)	48.6	9.2	5.2	5.2	31.8	9,35	0.12
SR (Nafta)	34.6	5.3	8.0	8.0	44.1	4.33	0.14
MBG (Coal)	52.2	29.5	5.6	4.4	5.1	9.32	0.34
FBG (Coal)	27.7	54.6	4.7	5.8	4.4	5.89	1.01
EFG (Goal)	26.7	63.1	1.5	0.03	2.0	17.80	1.13

65 SR = Stream reforming, MBG = Moving Bed Gasifier, FBG = Fluidized Bed Gasifier, EFG = Entrained Flow Gasifier

66

67 Traditionally, a separation unit is employed to produce the H_2-rich stream for power generation and CO_2

68 for carbon sequestration. More recently, investigations have suggested the re-use of sequestered CO_2

69 as fracking agent [4]. Alternatively, the integration of water gas shift reactors and separation in a single

70 unit has been intensively studied and referred to as sorption enhanced water gas shift (SEWGS) [5,6].

71 Dealing with highly pure H_2 streams raises concerns of safety during storage and transportation [7], and

72 poses new challenges for environmental and technological aspects during combustion [8], e.g.

73 production of pollutants such as NO_X [9]. On the other hand, the presence of CO_2 in the streams resulting

74 from shift reactors offers alternative technological solutions utilizing its effects as a thermal diluent.

75 Indeed, the use of CO_2 has been recently considered within the energy supply chain either as a service

76 fluid for indirect heat transfer or as a component in the combustion chamber for direct heat transfer [10].

77 The latter approach includes Allam's Cycle [11] and it can be intended as an integrated strategy to

78 recycle the CO_2 deriving from the carbon capture units and reduce the technical requirements. However,

79 if traditional, carbon-based fuels are considered, the presence of CO_2 alters the chemical equilibrium,

80 limiting the fuel conversion being a final product already present in the mixture. This drawback is

81   implicitly erased in the case of H_2-CO_2 mixtures. With these premises, direct combustion of H_2-CO_2

82   followed by carbon sequestration may be considered as a possible alternative, see Figure 1.
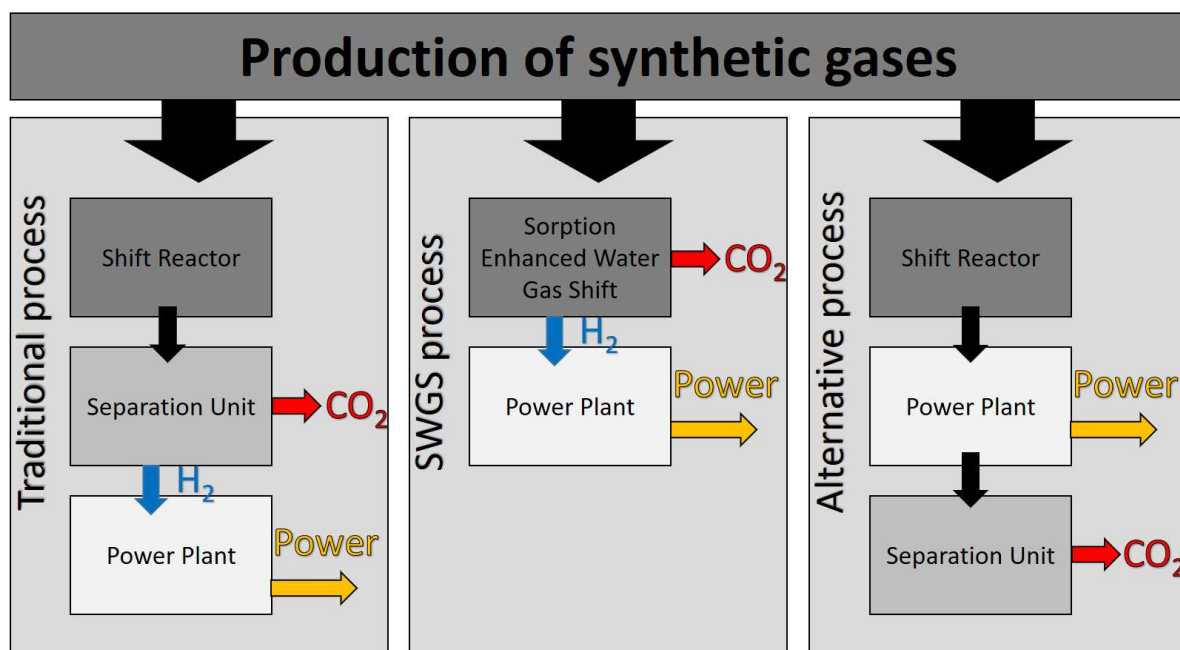
83   **Figure 1** Schematic representation of synthetic gas-based processes

84   Quantitative investigations on the chemistry of combustion and flammability limits of H_2/CO_2-

85   mixtures are missing at present. Indeed, most of the published studies dealing with the combustion

86   chemistry of binary mixtures of C_0-C_1 species were devoted to the characterization of the interactions

87   between CO and H_2 [12,13] in the view of synthetic gas utilization, or CH_4 and H_2 [14,15] for the

88   application of hydrogen enriched methane flames [16]. The chemistry of H_2-CO_2 in complex mixtures

89   was investigated as per the employment of oxygen-enriched air or pure oxygen [17] or in the case of

90   biomass-derived fuels [18–21]. For safety relevant aspects, the effects of CO_2 addition on the hydrogen

91   ignition limits were characterized by Djebaili et al. [22] at high temperatures, revealing the existence of

92   non-thermal inhibition of the hydrogen oxidation.

93   The laminar burning velocities (LBV) of H_2/CO_2- mixtures were investigated at different temperatures

94   and mixture compositions. For diluted H_2-air mixtures, planar flames formed in diverging channels could

95   be used for the measurement. The effect of CO_2 is stronger than that of N_2 in reducing the burning

96   velocity indicating a thermal and chemical effect of CO_2 dilution [23,24]. However, no apparent influence

97   on the morphology of the planar flame due to the CO_2 admixture is reported. In other studies with flat

98   flames, cellular structures were observed in CH_4, C_3H_8 and C_2H_6 flames [25] with high CO_2 dilution. Also

99   in flat flames stabilised on a McKenna burner, instabilities were observed in extremely lean CH_4-H_2-CO_2

4

100   flames with equivalence ratios of ϕ = 0.55-0.69. Beyond that, no further studies on instabilities of the

101   flame front due to the admixture of CO_2 are known [26]. The occurrence of cellular instabilities in

102   adiabatic $H_2/O_2/N_2$ premixed flames anchored to a heat flux burner has been investigated numerically.

103   Both hydrodynamic instabilities and diffusional instabilities leading to the formation of cellular flames

104   were studied [27]. An adiabatic unstretched planar flame anchored to the heat-flux burner could only be

105   realized within a critical lift-off distance. This lift-off distance seems to differ for each mixture. To explain

106   the occurrence of these phenomena in more detail, insights from experimental and numerical

107   investigations are necessary.

108   In this paper, H_2-O_2-N_2-CO_2 flames were investigated numerically to elucidate the effect of CO_2

109   dilution on combustion properties, flame structure and instabilities. The effects of CO_2 dilution on laminar

110   burning velocity and Markstein length are investigated and quantified with 1-D simulation results using

111   different reaction mechanisms. Further, the effects of CO_2-dilution on flame structure were investigated.

112   Significant changes in flame morphology were found in experiments with H_2-O_2-N_2-CO_2 flames stabilized

113   on a heat flux burner. The results were quantified as a function of plate temperature, unburned gas

114   velocity and equivalence ratio. 2-D numerical simulations served to explain the appearance of the

115   formation of cellular structures in the investigated flames.

116

1-D and 2-D Simulations, Numerical Setup and Procedure

118   Laminar burning velocity is generally considered a stand-alone parameter summarizing the

119   interaction of convection, diffusion and chemical reactions during combustion [28]. In this work, the

120   laminar burning velocity was estimated through the numerical simulation of one-dimensional, freely

121   propagating, and adiabatic flames with the open-source software Cantera [29]. Absolute and relative

122   tolerances for the steady-state problem were set to $1.0 \cdot 10^{-9}$ and $1.0 \cdot 10^{-4}$, respectively. Additional

123   information about the numerical setup and adopted procedure can be found elsewhere [30].

124   Several strategies for the development of detailed kinetic mechanisms can be used, including manual

125   enlargement or automatic generation [31]. The selected strategy as well as the approach adopted to

126   produce thermodynamic and kinetic data to be used as input strongly affect the laminar burning velocity

127   predicted by the produced mechanisms, as recently demonstrated [32]. Nevertheless, the identification

128   of the most accurate model for the hydrogen case is still a challenging task. Indeed, a comparison of

129   the experimental measurements for the laminar burning velocity of hydrogen-containing mixtures from

130   different setups shows a significant variability of this parameter [33]. On the other hand, it is worth

131 mentioning that all predictions can be included in the uncertainties range typically associated with the

132 laminar burning velocity measurements [34]. Eventually, the tendency of GriMech3.0 in underestimating

133 the overall reactivity has been already reported for low-carbon fuels [35].

134   A detailed kinetic mechanism composed of ~80 species and ~600 reactions, referred to as KiBO

135 (Kinetics in Bologna) was employed because of the verified accuracy in reproducing the combustion

136 chemistry of light species [28]. The initial temperature of T_{gas} = 298 K and atmospheric pressure were

137 considered. Several combustible mixture compositions were tested, varying the equivalence ratio

138 between ϕ = 0.5 - 6.0 and the H_2/diluent ratio by moles from 1.0 - 6.0. Either CO_2 or N_2 was used as

139 diluent. The same conditions were used for fictitious CO_2 (i.e., FCO_2), as well. FCO_2 is an artificial

140 species with the same thermodynamic and transport properties as CO_2, but not involved in any reaction.

141   A sensitivity analysis is performed by imposing a perturbation equal to 0.1 % of each input parameter

142 (i.e., the rate constant of the i-th reaction, k_i) and evaluating the effects on the LBV. Results are

143 expressed as normalized sensitivity coefficients (*NSC*), defined in Equation 2,

144 $$NSC = \left(\frac{k_{i,0}}{s_{L,0}}\right) \cdot \frac{\partial s_L}{\partial k_i} \qquad (2)$$

145 where the subscript 0 denotes the unperturbed values

146   Reaction path analysis identifies the key intermediates in the reaction path and quantifies the relative

147 weight of each branch by estimating branching ratios. The relative width of the connection pathway is

148 related to the relative contribution of the pathway to the species net yield [36]. In this work, a global

149 pathway selection algorithm is implemented in a zero-dimensional constant volume system to identify

150 the shortest paths connecting the most relevant species involved in the element flux. A threshold value

151 of 0.01 is adopted for the selection of species to be included in the analysis. This approach allows for

152 the generation of overall reaction paths. Hence, results are independent of the time instance, in contrast

153 to the traditional path flux algorithm. Considering the analysed mixtures, the migration of H is

154 investigated. Additional details of this methodology can be found in the references [37,38].

155   The effect of carbon dioxide dilution of hydrogen on possible thermo-diffusive instabilities is

156 numerically investigated using one-dimensional and two-dimensional flames. In this context, the

157 Markstein number Ma expresses how sensitive the burning velocity s_L, normalized by the flame speed

158 of an unstretched flame $s_{L,0}$, is to the dimensionless flame stretch or Karlovitz number Ka:

159 $$Ma := -\frac{\partial s_L/s_{L,0}}{\partial Ka} \qquad\qquad Ka := \frac{1}{A}\frac{dA}{dt}\frac{d_{fl,0}}{s_{L,0}} \qquad (3)$$

160   where $d_{fl,0}$ is the thermal thickness of the unstreched flame front. A negative Markstein number is

161   generally indicative of thermo-diffusively unstable flames. To quantify the Markstein number of hydrogen

162   flames with different fuel dilutions, numerical simulations of counterflow-twin flames are performed with

163   the open-source library Cantera [29]. In this axisymmetric setup, two opposed nozzles in 5 cm distance

164   serve as inlets of the premixed hydrogen-dilutant-air mixture at atmospheric conditions with a prescribed

165   velocity. The oxidizer is air and the fuel is a mixture of hydrogen and the dilutant. In all cases, the

166   equivalence ratio is $\phi = 0.9$. The diffusion model is the mixture-averaged model applying the

167   Hirschfelder-Curtiss approximation, thereby taking preferential diffusion into account.

168   Lastly, a detailed 2-D simulation of a spherically expanding flames is conducted to study the

169   evolution of cellular structures on the thermo-diffusively unstable flame during flame propagation.

170

171

172   **Numerical results**

173   **Laminar Burning Velocity, Non-Stretched Flames**

174   The effects of the CO_2 share in the unburnt mixture on the laminar burning velocity estimated at

175    $T_{gas} = 298$ K and $p_{gas} = 1$ bar are reported in Figure 2 in dependence on the equivalence ratio. The case

176   where N_2 was added to H_2 is included for comparison.
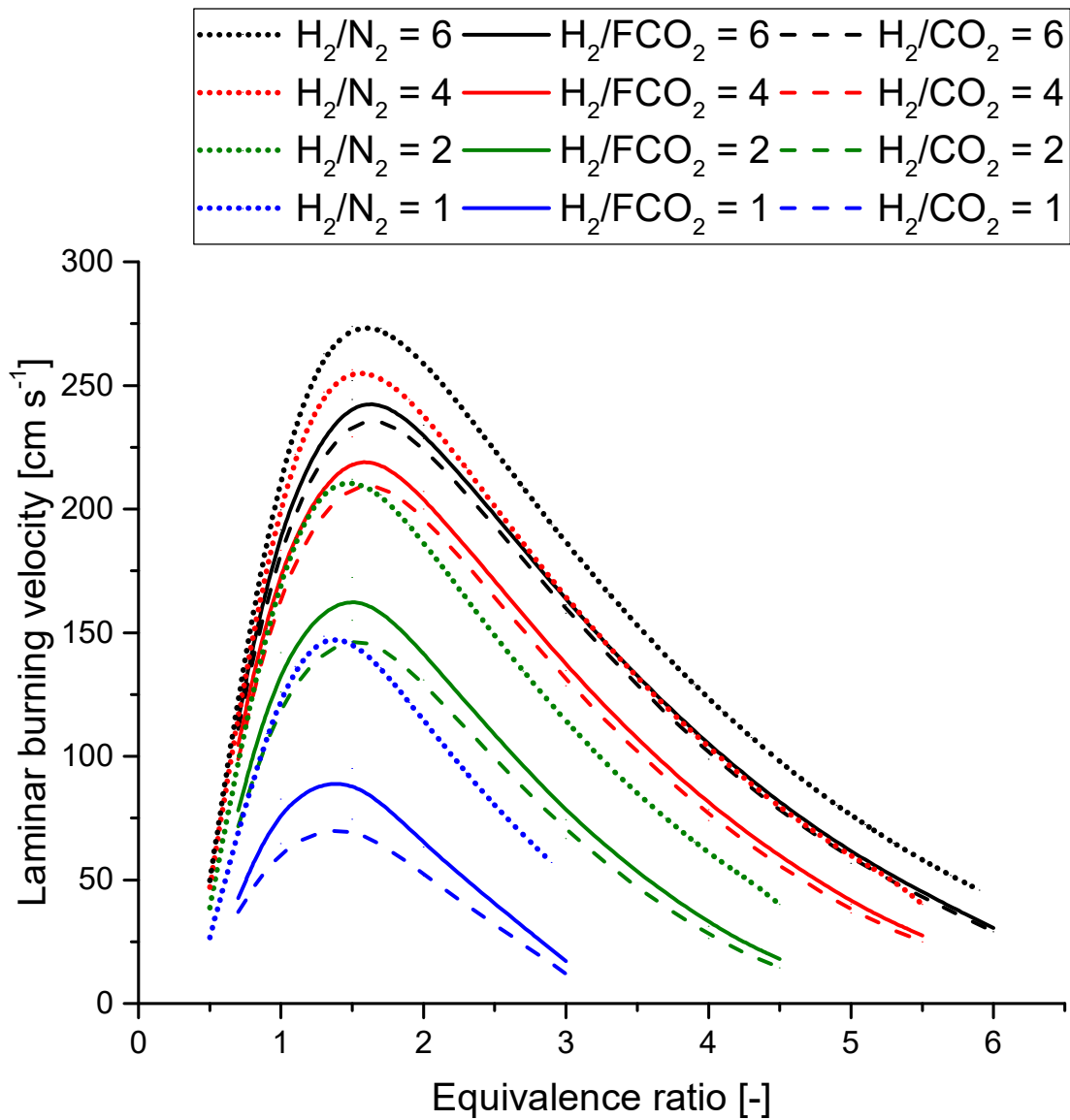
177

Figure 2 Comparison of estimated LBV at 298 K and 1 bar, in dependence on the equivalence ratio (the notation X/Y stands for the volume ratio).

178

179   The introduction of FCO_2 has a significant effect regardless of the H_2/CO_2 ratio increasing the

180   laminar burning velocity compared with CO_2, especially at near-stoichiometric compositions. The

181   reduced overall burning velocity testifies to the chemical effects of CO_2. FCO_2 can be viewed as

182   accounting for the thermal dilution only. The estimated laminar burning velocities of H_2/FCO_2 and H_2/N_2

183   mixtures show significantly larger values for the second case, regardless of the equivalence ratio and

184   fuel composition considered. For example, the increase in the fundamental laminar burning velocity

185   achieves values up to 50% for elevated dilution (i.e., low H_2/FCO_2 H_2/N_2 ratios). This trend can be

186   explained considering the thermal inertia of the adopted diluents. It is worth noting that the observed

187   increase in the laminar burning velocity can be linearly associated with the variation of the average heat

188   capacity ($\overline{c_p}$), namely $LBV_{H_2/N_2}/LBV_{H_2/FCO_2} \approx \overline{c_p}_{H_2/N_2}/\overline{c_p}_{H_2/FCO_2}$. On the other hand, the magnitude of the

189   effects of the chemistry of CO_2 on the LBV is largely influenced by the applied compositions. Indeed,

190   the variation in the laminar burning velocity is limited to -10% for lean compositions, whereas it can

191   reach ~-25% at stoichiometric and ~-40% in rich conditions. This trend is in line with the increased

192   contribution of radicals in the conversion of the fuel typically attributed to the increase in equivalence

193   ratios [39]. Considering the structure of the adopted mechanism, CO_2 plays either a direct role as a

194   reactant/product dependent on the concentration or an indirect role as a diluent. The reaction associated

195   with the formation of CO_2 via CO oxidation (i.e., $CO + OH \leftrightharpoons CO_2 + H$) is a clear example of the above-

196   mentioned direct role. The presence of CO_2 alters the equilibrium, suppressing the formation of H

197   radicals, thus potentially affecting the reactivity of the whole system. Conversely, reactions where CO_2

198   acts simply as inert diluent reducing the reaction rate by decreasing the reactant concentrations can be

199   included into the group of indirect contributions.

200   For further clarification, the relevance of each reaction of the adopted mechanism was assessed

201   through a sensitivity analysis. Although larger relative deviations between the dilution with FCO_2 and

202   CO_2 are observed in rich compositions, the stoichiometric composition shows the largest absolute

203   differences. Hence, the sensitivity analysis performed in this work was executed at 298 K, 1 bar, and

204   stoichiometric composition (Figure 3) to assess the effect of CO_2 on the most influential reactions. For

205   the sake of clarity, reactions are sorted by the absolute values of the NSCs and only the largest ten are
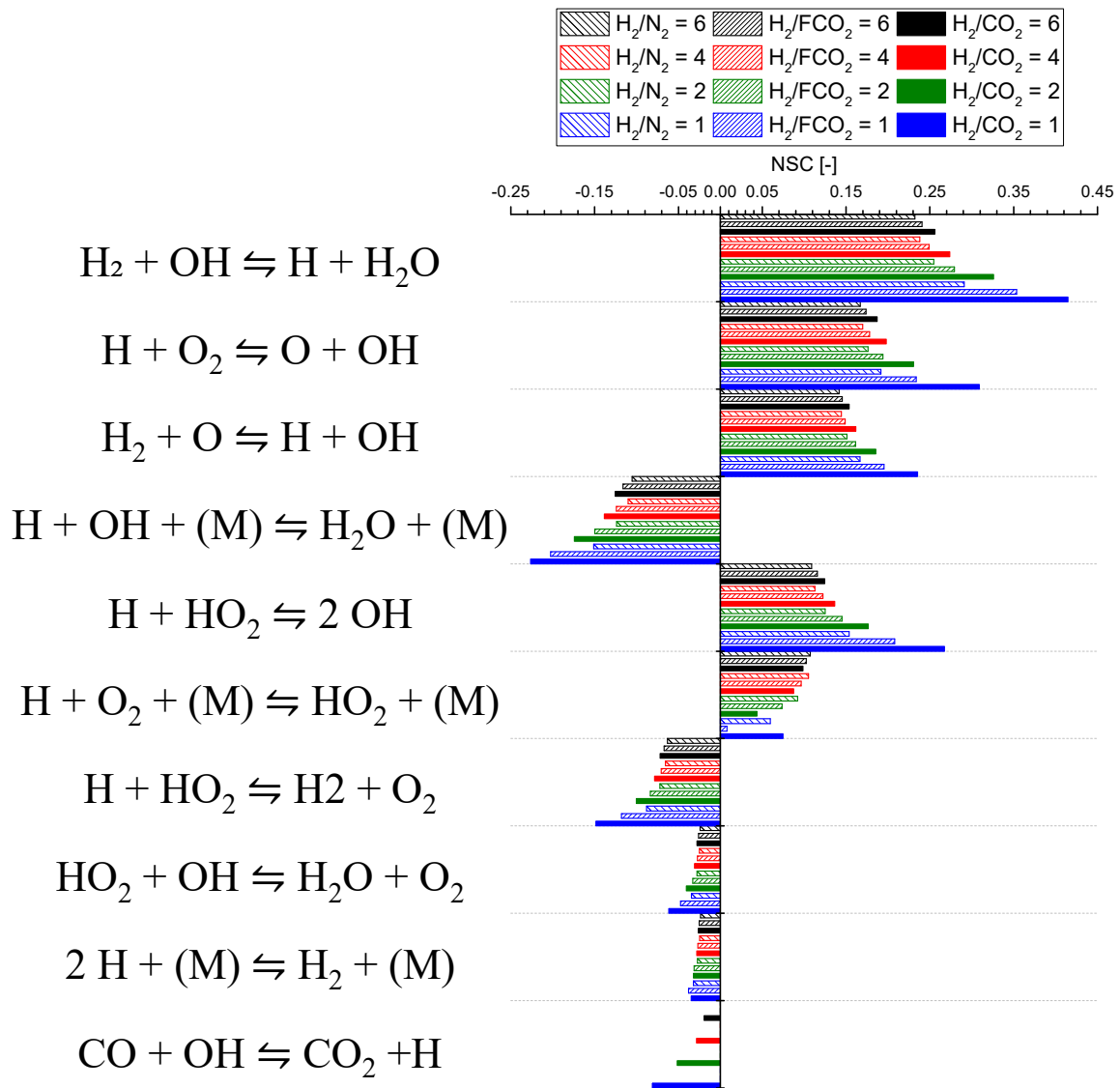
206   listed.

207

Figure 3 Comparison of normalized sensitivity coefficients of the laminar burning velocity with respect to the rate constants at 298 K and 1 bar, as a function of the initial fuel composition at stoichiometric conditions (the notation X/Y stands for the volume ratio).

208

209   Regardless of the chemical and thermal properties of the diluent, increasing the H_2 content leads to a

210   general decrease in the absolute value of the NSCs. Besides, the comparison between the values for

211   the FCO_2 and N_2 dilution shows slightly lower values for the latter case, except for the $H + O_2 + (M) \leftrightarrows$

212    $HO_2 + (M)$ reaction. This reaction represents the only case of a falloff reaction having CO_2 efficiencies

213   lower than that of H_2 among the ones reported in Figure 3. This observation suggests that the

214   competition between CO_2 (or FCO_2) and H_2 has a detrimental effect on $H + O_2 + (M) \leftrightarrows HO_2 + (M)$.

215 Conversely, the direct role of CO_2 can be evaluated through the comparison between the CO_2 and FCO_2

216 data. In most cases, larger NSCs are calculated for CO_2 dilution for a given fuel composition. These

217 trends imply that the presence of CO_2 makes the systems more sensitive to the chemistry of OH and H

218 radicals either from a kinetic or thermal point of view. It should be noted that the most influential reaction

219 directly involving CO_2 is $CO + OH \leftrightarrows CO_2 + H$. NSCs corresponding to the FCO_2 and N_2 cases are

220 negligible for this reaction due to the inert character of these reactants. Hence, the presence of CO_2 can

221 promote the formation of CO and OH through the reverse reaction, consuming H. Besides, this reaction

222 offers the possibility to explain the differences in laminar burning velocities, as the NSC is negative and

223 the reaction is typical of near stoichiometric mixtures. These observations can be confirmed by the

224 reaction path analysis shown in Figure 4 for equimolar fuels (i.e., H_2/CO_2 and H_2/FCO_2 equal to 1) under

225 flame conditions, namely 1200 K, 1 bar, and stoichiometric mixture composition.

226
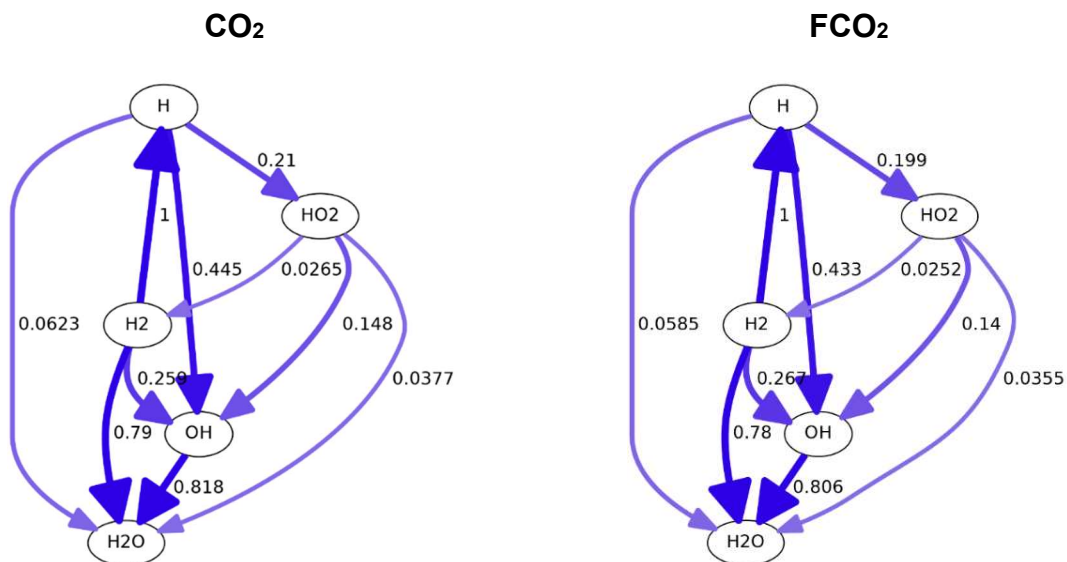
227 **Figure 4.** Reaction path analysis for CO_2 and FCO_2 in equimolar composition with H_2 and

228 stoichiometric conditions at initial temperature 1200 K and 1 bar.

229 Although the general structure of the presented reaction paths is not affected by the fuel composition,

230 significant variations in branching ratios can be observed. The flux diagrams indicate that the presence

231 of CO_2 slightly affects the relative contribution of branches producing small radicals, except for the direct

232 production of H. Looking at the intermediates resulting from primary reactions involving H_2, OH is

233 favoured by FCO_2 to the detriment of direct H_2O formation. Combining these observations with the

234 results of the sensitivity analysis, it is obvious that CO_2 affects the competition between $H_2 + O \leftrightarrows H +$

235   OH and $H_2 + O + (M) \leftrightharpoons H_2O + (M)$. It should be noted that CO_2 and FCO_2 have the same collision

236   efficiencies for any third body reaction included in the mechanism, leaving the reaction rate of $H_2 + O +$

237    $(M) \leftrightharpoons H_2O + (M)$ unaffected. Therefore, the abovementioned differences can be mainly attributed to the

238   difference in temperature due to the modified global heat release of the systems. The resulting excess

239   in OH suppresses its production from H and HO_2, mostly attributable to $H + HO_2 \leftrightharpoons 2\ OH$. Following the

240   observations derived from the sensitivity analysis, the branch connecting H to OH is diminished by about

241   3% at the investigated conditions through FCO_2 with the chemical contribution from $CO + OH \leftrightharpoons CO_2 +$

242   H.

243

244   **Laminar Burning Velocity, Stretched Flames**

245   To investigate the effect of CO_2 dilution on the burning velocity of stretched flames and possibly

246   flame instabilities a one-dimensional counterflow flame is considered. The setup consists of two

247   opposed nozzles with identical premixed hydrogen-dilutant-air mixtures at atmospheric conditions.

248   Three cases at $\phi = 0.9$ are considered, where the fuel consists of a) pure hydrogen, b) 30 mol-%

249   hydrogen and 70 mol-% CO_2, and c) 30 mol-% hydrogen and 70 mol-% nitrogen. All cases are

250   computed using the DRM19 reaction mechanism [40], which has been used in the literature for similar

251   conditions, and the KiBO mechanism. Figure 5 shows the burning velocity over Karlovitz number, which

252   represents the non-dimensional flame stretch (see equation 3) for the different fuel mixtures. The flame

253   with pure hydrogen as a fuel has a positive Markstein number, which is indicative of a thermo-diffusively

254   stable flame. The flame with nitrogen dilution has a Markstein number close to zero and is therefore

255   insensitive to flame stretch. The flame with CO_2 dilution on the other hand has a negative Markstein

256   number.
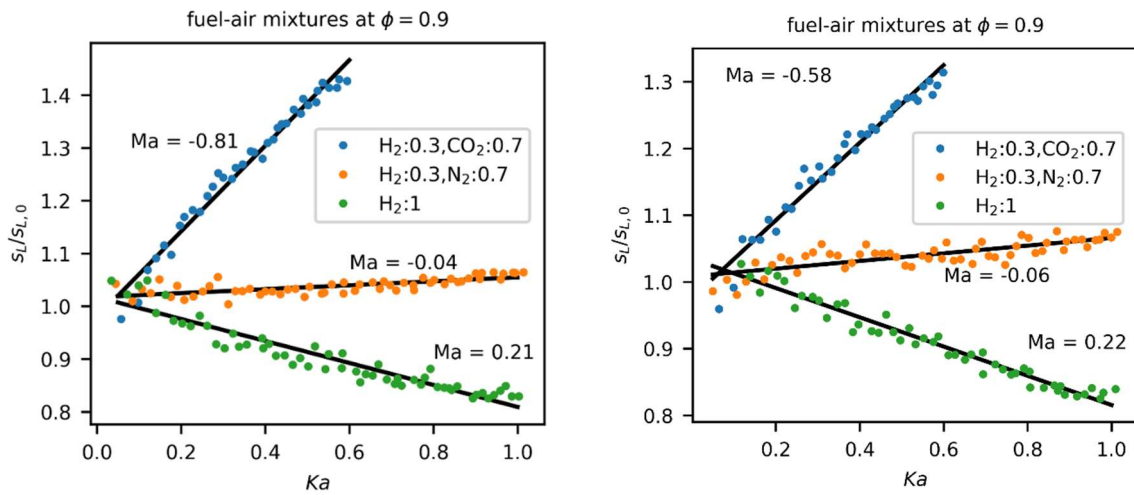
Figure 5 Burning velocity over Karlovitz number from the twin-counterflow flames for different fuel mixtures and resulting Markstein numbers. Left: DRM19 reaction mechanism. Right: KiBO reaction mechanism.

The reason for the negative Markstein number resulting from the CO_2 dilution is mainly attributed to the reduction of the thermal diffusivity of the gas mixture and therewith the reduction of the Lewis number. The thermal diffusivity of the fuel-oxidizer mixture with pure hydrogen at $\phi = 0.9$ is $a = 4.5 \times 10^{-5}$ m²/s, while the mixture thermal diffusivity with CO_2 dilution is $a = 2.9 \times 10^{-5}$ m²/s. The simulation with CO_2 dilution has been repeated by replacing CO_2 with the chemically inert FCO_2. Disabling the conversion of CO_2 leads to slightly higher burning velocities and a slightly larger Markstein number ($Ma = -1.0$), but otherwise the same trend is found. Likewise, changing the diffusion model from the mixture-averaged model to the multi-component model including the Soret effect yields a similar Markstein number of -0.99 for the H_2-CO_2 mixture and +0.21 for the pure hydrogen flame (compare with Tab. 2).

To validate these results, simulations of cases a) and b) have been repeated with the detailed GRI 3.0 reaction mechanism [41] and the reduced reaction mechanism by Kee [42]. For the pure hydrogen flame, the reaction mechanisms by Li et al. [43], Konnov [44], and Connaire et al. [45] were included in the comparison as well. While there are slight differences in the predicted burning velocity and Markstein number, they all show the same tendency, i.e. a change from a flame with $Ma > 0$ for pure hydrogen as fuel to a flame with $Ma < 0$ when considering dilution with CO_2. The results are summarized in Table 2. Flames with $Ma < 0$ are potentially thermo-diffusively unstable. It should be noted that the GRI3.0

13

278   reaction mechanism has not been originally validated for methane-hydrogen blends and thus shows

279   considereable differences in flame speed compared with other reaction mechanisms, especially for case

280   b. Nonetheless, we included it here because GRI3.0 is still widely used today. Even though the

281   prediction of the laminar flame speed differs, the observed trend of CO_2 addition stays the same: the

282   Markstein number of the reactive mixture changes from positive to negative, showing that the addition

283   of CO_2 leads to a thermodiffusively unstable flame.

284

285

286   **Table 2** Burning velocity and Markstein number from the twin-counterflow flames obtained

287   with different reaction mechanisms at ϕ = 0.9

288

Case a (100 mol-% H_2)

Mechanism	$s_{L,0}$ (m/s)	Ma
DRM19	2.24	+0.21
KiBO	2.12	+0.22
GRI3.0	2.02	+0.33
Kee	2.21	+0.32
Li	2.02	+0.30
Konnov	2.03	+0.33
Connaire	1.97	+0.28

Case b (30 mol-% H_2, 70 mol-% CO_2)

| Mechanism	$s_{L,0}$ (m/s)	Ma
DRM19	0.111	-0.81
KiBO	0.107	-0.58
GRI3.0	0.066	-1.07
Kee	0.138	-0.74

289

290

291   **Experiments for determining of the flame front instabilities**

292   As stated above, flames with $Ma < 0$ are potentially thermo-diffusively unstable. To investigate

293   thermo-diffusive instabilities and non-stable flame fronts, a flat flame burner with a stabilized flame was

294   selected also allowing optical examination of changes in the flame front over long examination intervals.

295   These burners are usually used to determine the laminar burning velocity of quasi-adiabatic flat flames.

296   The heat flux burner design used in the present work was proposed by de Goey et al. [46], based on

297   the fundamental experimental work done by [47]. The method has the advantage of directly measuring

298   the LBV of a planar stationary unstretched flame. The stabilization of a planar flame has been further

299   proved by [48] and can be achieved with a temperature-controlled burner plate compensating heat

300   losses from the flame. In the experimental setup used here the gas flow is controlled by three calibrated

301   mass flow controllers (MFCs). The ambient conditions as well as the signals from newly integrated type

302   T thermocouples are recorded and used to calculate the LBV [49]. By definition, the determination of

303   the laminar burning velocity is only possible for planar flames. Therefore, the radial temperature profiles

304   of the plate are analysed for up to 350 measurements to find conditions for adiabatic stabilisation of the

305   flame, i.e. the parabolic coefficent C of the radial temperature profile equals 0, see middle of figure 6.

306   For further details of the setup [50,51] and experimental uncertainties [52] related to gas flows and other

307   possible sources of errors, refer to Eckart et al. [53–56] and Rau et al. [57]. If instabilities and cellular

308   structures occur, a determination of the LBV is not permissible.
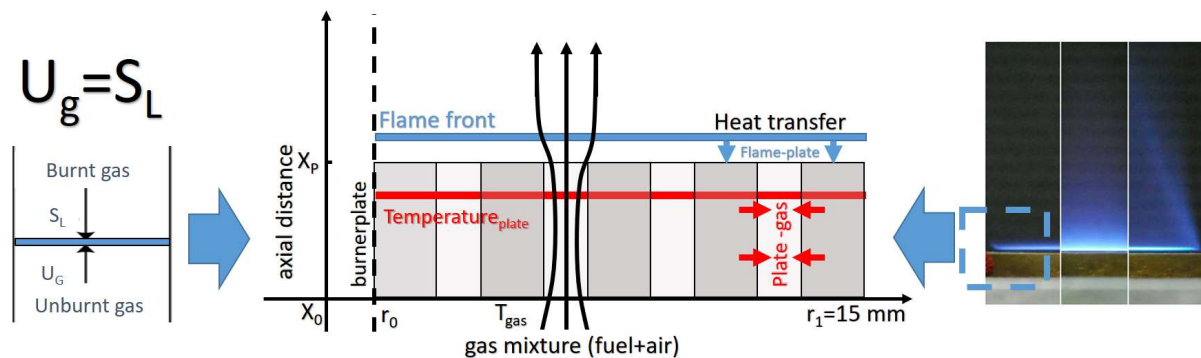
309   **Figure 6** Schematic drawing of the heat flux burner setup and the position of the stabilized

310   flame.

311   Experiments are conducted at equivalence ratios ($\phi = 0.5$–1.1) and CO_2 contents up to 70% in

312   hydrogen. The initial gas temperatures are 300 K. Under these conditions, cellular structures could be

313   observed. To evaluate the behaviour of the flames and their instabilities, a VIS-camera was mounted

314   above the heat flux burner. With this optical setup, 10 pictures of the stabilized flame were taken at a

315   time interval of 120 s. These pictures were then evaluated carrying out a step binarization and reduction

316   of small interference effects due to reflections. Subsequently, edge detection and a watershed were

317   performed in a parameterized manner. This procedure made it possible to separate flame structures

318   from each other. The number of separated flames was evaluated and displayed graphically as an

319   overlay. The procedure can be seen step by step in Figure 7.

320

a)   b)   c)   d)
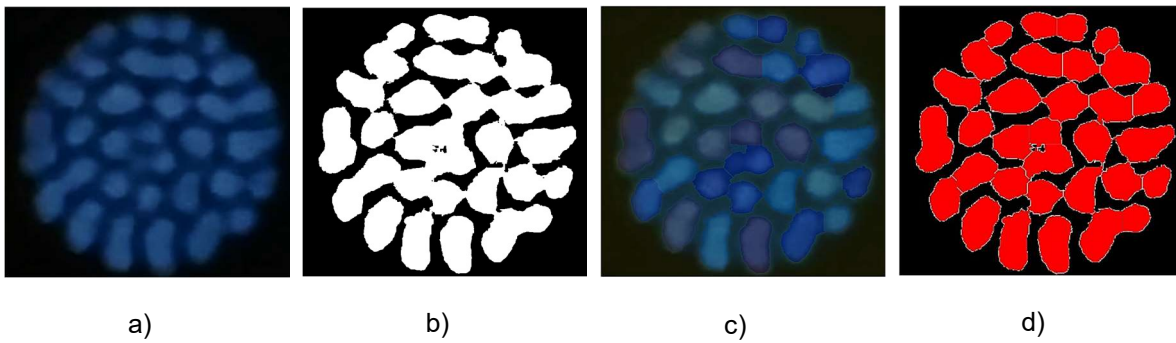
321   **Figure 7** Steps of image processing, a) raw data of the heat flux flame, b) binarization and

322   reduction of reflections, and c) overlay of detected watersheded cells and d) counting.

323

324   **Experimental results for flame structures**

325   Experimental results obtained at atmospheric pressure for hydrogen-carbon dioxide-air mixtures at

326   various equivalence ratios of ϕ = 0.5 - 1.1 were analyzed. Figure 8 shows the comparison of measured

327   unburnt gas velocity and the parabolic coefficient C for equivalence ratio ϕ = 0.9 and a flame with 30 mol-

328   % hydrogen diluted by 70 mol-% of CO_2. In the experiments, different plate temperatures (368-428 K)

329   were applied. It was observed that the plate temperatures affect the parabolic coefficient, which is

330   normally used to interpolate to the adiabatic state. The overall trend of the results was not influenced by

331   the plate temperature. Since all the flames were not planar and therefore did not correspond to the

332   theoretical prerequisites for the determination of the laminar burning velocity, the inflow velocity cannot

333   be considered the same as the burning velocity even if the parabolic coefficient is C = 0. The

334   determination of the laminar adiabatic curvature and stretch free burning velocity was not possible for

335   the investigated regions, as impairments were detected in the flame in all cases. In the experiments, it

336   could be shown that with an increase in the velocity at the outlet and a corresponding increase in the

337   volumetric flow rate, the temperature in the middle of the plate decreased in the order of $\Delta T_{max} \approx 15K$.

338   These changes also had no influence on the flame shape of the H_2-O_2-N_2-CO_2 flames.
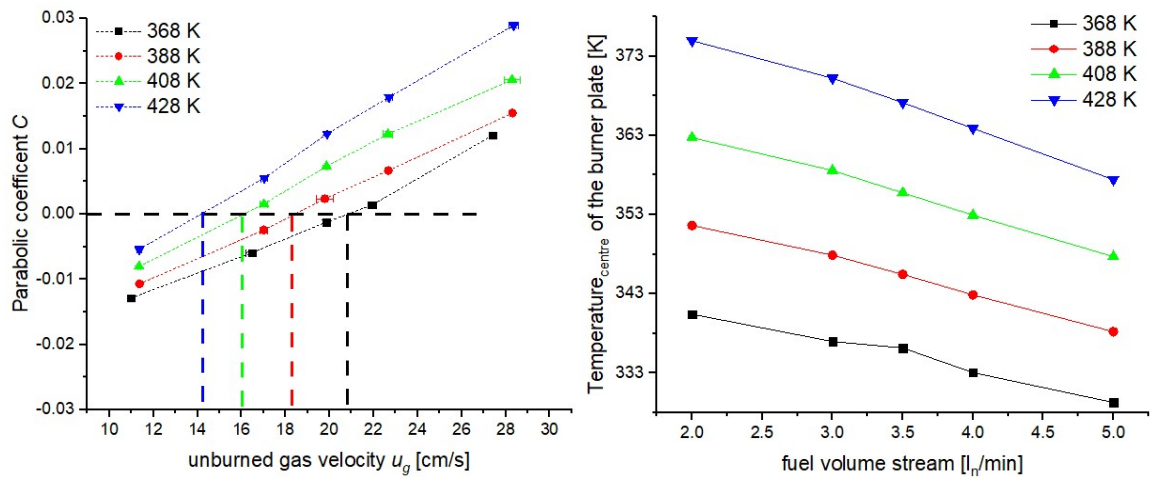
Figure 8 Measured parabolic coefficient and fuel volume stream as a function of plate temperature for a flame with 30 mol-% H_2 diluted by 70 mol-% of CO_2, for equivalence ratio $\phi = 0.9$ and $T_{gas} = 300$ K

339   In Figure 9 the flame morphology with view from above and from the side at the plate temperature of

340    $T_{plate} = 368$ K and varying flow rates are illustrated. The flames have been operated with 30 mol-%

341   hydrogen diluted by 70 mol-% of CO_2 at an equivalence ratio $\phi = 0.9$ and $T_{gas} = 300$ K. It can be seen

342   that the intensity of the individual flame structures increases significantly with inflow velocity. With

343   increasing inflow velocity, the flames are also stabilized further away from the burner plate and a

344   "sealed" flame front is no longer appearing. The change of this state can be seen in the range from 3 to

345   4 l_n/min, whereby the transition from negative to positive parabolic coefficients can also be detected (see

346   Figure 8).
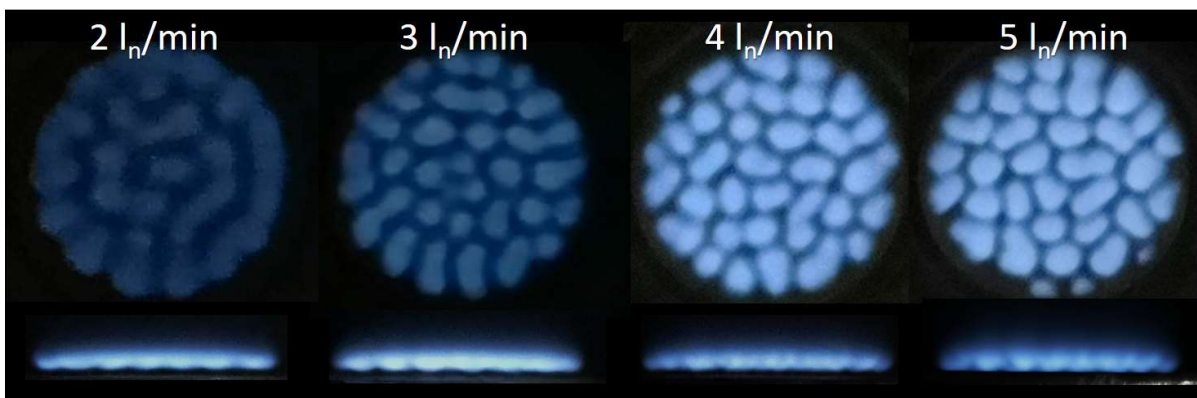
347   **Figure 9** Flame morphology for different volume streams with 30 mol-% hydrogen and

348   70 mol-% carbon dioxide for an equivalence ratio of $\phi = 0.9$, $T_{gas} = 300$ K and $T_{plate} = 368$ K,

349   top: top view, bottom: side view

350   For two different image series, one depending on the fuel flow and one on the equivalence ratio, the

351   number of cells in the broken flame front was analysed. The series were recorded independently of each

352   other. However, it can be seen that both overlap in the uncertainties regions. The maximum number of

353   cells is again located in the range of parabolic coefficients around $C = 0$. The number of cells is in the

354   same order of magnitude as found by Konnov et al. for methane flames, but below the ones of ethane

355   and propane flames. In this study, however, "closed" flame fronts were frequently found [25]. For the

356   highest volume flow rate tested, an evaluation of the number of individual cellular flames as a function

357   of the equivalence ratio was carried out according to the procedure described above. It turns out that a

358   maximum of around 45 cells could be found, as seen in Figure 10 b). Konnov et al. [25] could find the

359   maximum cell count for methane flames in the range of $\phi = 0.8$, whereas for ethane and propane higher

360   values were observed at $\phi = 1.2$-1.4 and 1.3, respectively.

361

a)   b)
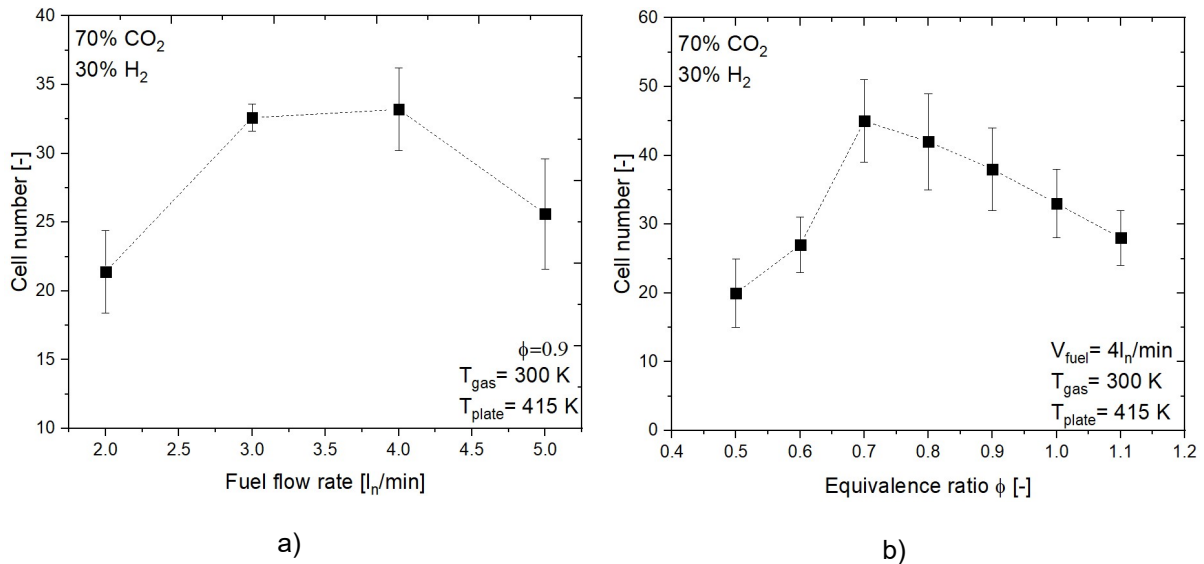
362   **Figure 10** Cell number a) depending on the fuel flow rate and b) the equivalence ratio

363   **2-D Numerical Simulation of Spherically Expanding Flames**

364   To investigate the thermo-diffusive instabilities caused by the CO_2 dilution further and to assess the

365   structure of the flames, detailed simulations of spherically expanding, constant pressure flames in

366   initially quiescent premixed fuel-air mixtures at atmospheric conditions ($p = 1\,\mathrm{atm}, T = 300\,\mathrm{K}$) are

367   conducted. A H_2-air (case a, $\phi = 0.9$, 100 % H_2) and a H_2/CO_2-air flame from case b ($\phi = 0.9$, 30 mol-

368   % H_2 and 70 mol-% CO_2) are simulated. The computational setup consists of a quasi-3D domain, which

369   is a wedge-shaped half-sphere, as shown in Figure 11. For the flame of case a, the diameter of the

370   computational domain is 16 cm and the mesh consists of 8.1 million finite volumes, yielding a resolution

371 in the equidistant region of the mesh of 33 μm. For the CO_2 diluted flame of case b, the diameter of the

372 domain is 48 cm and consists of 65 million finite volumes with a resolution of 56 μm. The finer mesh for

373 the flame in case a is required due to the pure hydrogen flame having a lower flame thickness. Similarly,

374 the flame speed of the CO_2 diluted flame is lower, and therefore a larger propagation distance is required

375 for the flame to develop the thermo-diffusive instabilities. In both cases, the flame zone is fully resolved

376 with more than 15 cells.

377
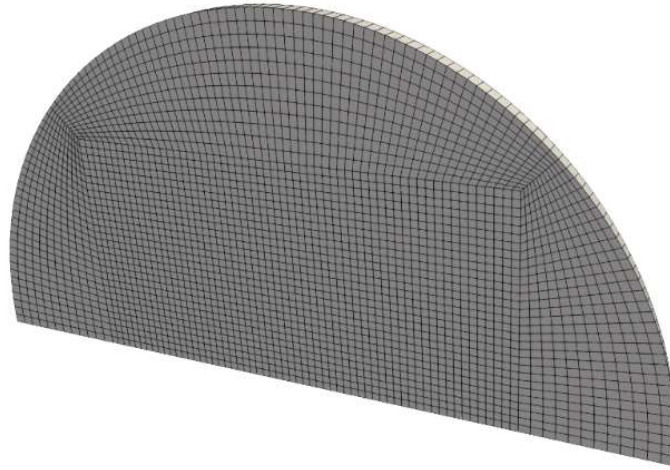
378 **Figure 11** Computational domain for the spherically expanding flames

379 The simulation is performed with an in-house solver for the detailed simulation of flames [58–60]

380 based on OpenFOAM [61] and Cantera, which has been validated in previous works [62–65]. It solves

381 the fully compressible Navier-Stokes equations together with a balance equation for energy and each

382 chemical species. The conservation of total mass reads

$$\frac{\partial \rho}{\partial t} + \nabla \cdot (\rho \vec{u}) = 0 \tag{4}$$

383 ρ is the density, t time and $\vec{u}$ is the gas velocity. The conservation of momentum is expressed as

$$\frac{\partial (\rho \vec{u})}{\partial t} + \nabla \cdot (\rho \vec{u} \vec{u}) = -\nabla p + \nabla \cdot \tau \tag{5}$$

384 with p the pressure and τ the stress tensor

$$\boldsymbol{\tau} = \mu \left(\nabla \vec{u} + \nabla \vec{u}^{\mathrm{T}} - \frac{2}{3} \nabla \cdot \vec{u} \boldsymbol{I} \right) \tag{6}$$

385 and μ being the dynamic viscosity of the reacting mixture. $\boldsymbol{I}$ is the unit tensor. The balanance of species

386 masses is expressed in terms of the mass fractions Y_k of species k

$$\frac{\partial(\rho Y_k)}{\partial t} + \nabla \cdot (\rho \vec{u} Y_k) = \dot{\omega}_k - \nabla \cdot \vec{j}_k \qquad (7)$$

387   where $\dot{\omega}_k$ is the reaction rate of species k and $\vec{j}_k$ its diffusive flux. Species diffusion is computed from a

388   mixture-averaged approach

$$\vec{j}_k = -\rho D_k \nabla Y_k \qquad (8)$$

389   where D_k is the diffusion coefficient of species k computed from kinetic gas theory. The energy balance

390   is formulated in terms of the total sensible enthalpy:

$$\frac{\partial(\rho(h_s + \frac{1}{2}\vec{u} \cdot \vec{u}))}{\partial t} + \nabla \cdot (\rho \vec{u}(h_s + \frac{1}{2}\vec{u} \cdot \vec{u})) = -\nabla \cdot \vec{q} + \frac{\partial p}{\partial t} - \sum_k h_k^\circ \dot{\omega}_k \qquad (9)$$

391   h_k° is the enthalpy of formation of species k and h_s the sensible enthalpy of the mixture. $\vec{q}$ is the diffusive

392   heat flux

$$-\nabla \cdot \vec{q} = \nabla \cdot \lambda \nabla T - \sum_k \nabla \cdot h_{s,k} \vec{j}_k \qquad (10)$$

393   where λ is the heat conductivity of the gas mixture, T ist the temperature and $h_{s,k}$ the sensible enthalpy

394   of species k.

395   The DRM19 reaction mechanism is used and chemical reaction rates are computed from finite rate

396   chemistry. The diffusion model is the mixture-averaged model. For time discretization, a second order

397   implicit method is used, while spatial discretizations are computed with fourth-order interpolation

398   schemes. The initial condition is given by a spherical flame kernel with a radius of 2 cm, obtained from

399   a one-dimensional pre-cursor simulation of a spherically expanding flame. The subsequent flame

400   propagation and development of instabilities is then captured during the simulation in detail.

401   Figure 12 shows the temporal evolution of the flame front for the hydrogen-CO_2 fuel mixture of case b

402   during flame propagation in terms of the heat release rate (HRR) at different time instances. The flame

403   starts from a perfectly spherical configuration. While the flame expands, cellular structures form on the

404   flame front. The red box indicated in the top figure is later discussed in Figure 14.

405   At negatively curved parts of the flame front, the flame locally extinguishes, which is consistent with

406   the negative Markstein number. The structure of the cell formation follows the typical flame finger

407   configuration [66]. In this way, the H_2-CO_2 flame at $\phi = 0.9$ behaves the same as thermo-diffusively

408   unstable, lean ($\phi \ll 1$) pure hydrogen flames [67].
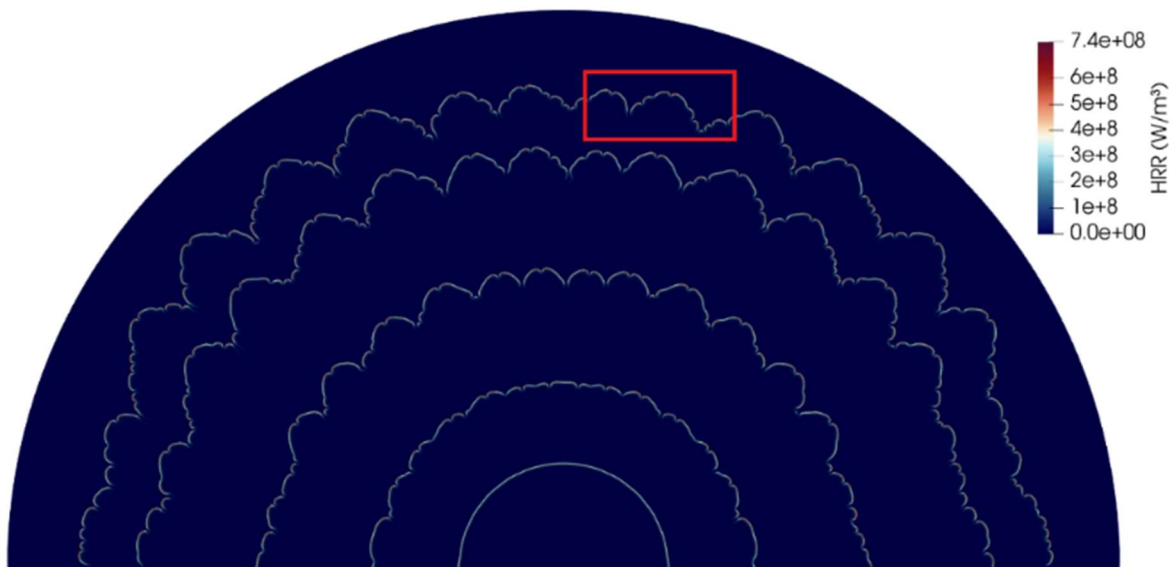
Figure 12 Flame front indicated by the heat release rate (HRR) at different time instances for

the flame from case b during spherical propagation.

Figure 13 shows the propagating pure hydrogen flame at $\phi = 0.9$, again in terms of heat release rate

at different time instances. As the flame reaches a sufficient radius, it becomes corrugated. However,

this corrugation is not an effect of thermo-diffusively unstable cellular structures, but a hydrodynamic

instability due to thermal expansion across the flame front (Darrieus-Landau instability), lacking the

typical structure of the flame fingers or thermo-diffusive cells. This distinction is shown more clearly in

Fig.14.
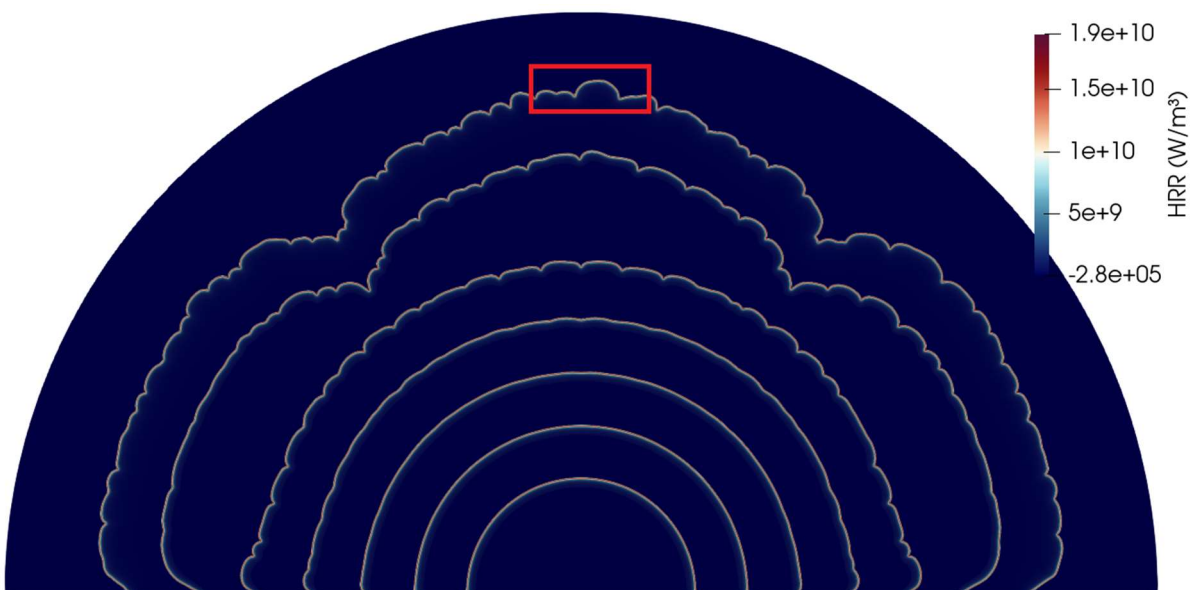
Figure 13 Flame front indicated by the heat release rate (HRR) at different time instances for

the flame from case a during spherical propagation.

419

420   The reaction zones indicated by the red boxes from Fig. 12 and 13 are zoomed-in in Fig. 14. The top

421   figure shows the CO_2 diluted flame. Due to the cellular structures caused by the thermo-diffusive

422   instability, characteristic flame fingers develop [66]. These also have a characteristic length scale, in this

423   case with a diameter of about 3 cm. The depicted heat release rate field also shows that the flame locally

424   extinguishes at the negative curved parts of the flame front, and locally enhances at the positively curved

425   parts of the flame front. This is in accordance with the negative Markstein number, as computed from

426   the one-dimensional counterflow flame simulations. In this way, the H_2-CO_2 flame at $\phi = 0.9$ behaves

427   the same as thermo-diffusively unstable, lean ($\phi \ll 1$) pure hydrogen flames [67].

428   On the other hand, the zoom into the flame front of the pure hydrogen flame at $\phi = 0.9$ does not

429   show the typical cellular structure of thermo-diffusively unstable flames. Instead, the corrugations on the

430   flame front are irregular, eventually forming cusps consistent with hydrodynamic instabilities. Again, in

431   accordance with the low positive Markstein number from Table 2, the correlation of local heat release

432   rate and flame curvature is reversed: in this case, the local heat release rate becomes maximal at the

433   negatively curved parts of the flame front. Since the Markstein number is close to zero, the sensitivity of

434   local flame speed or heat release rate with respect to flame curvature is low. Therefore, the variation of

435   HRR along the flame front is low and no local extinction occurs.
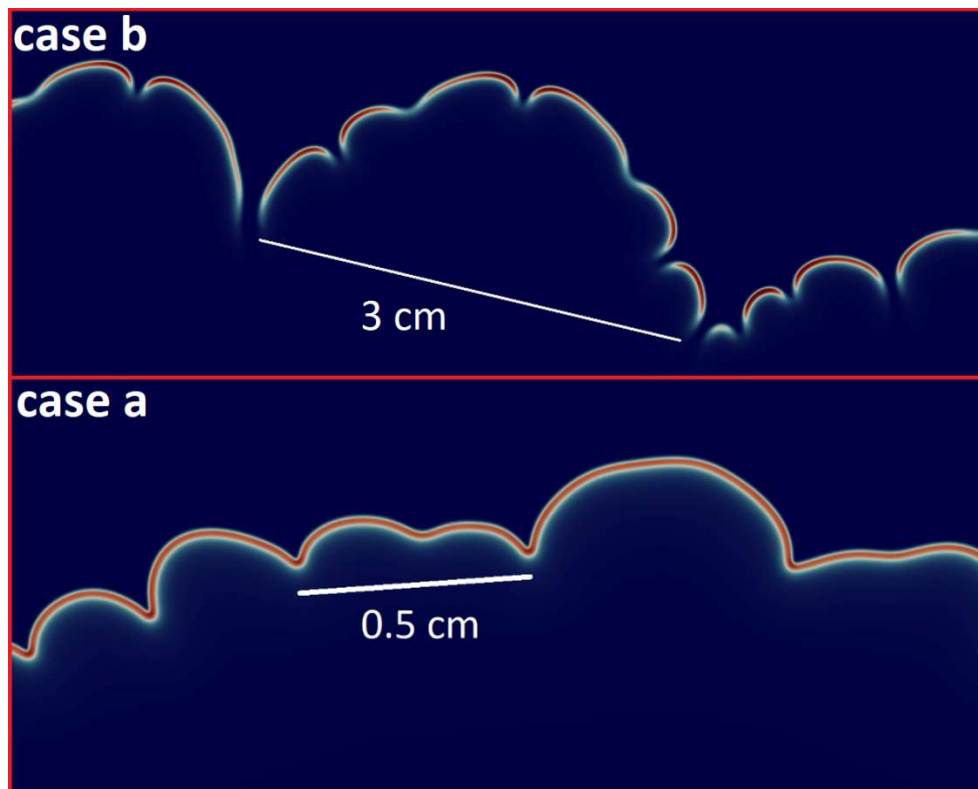
436   **Figure 14** Zoomed-in regions from Fig. 12 and 13. Top: heat release rate field from the CO_2

437   diluted flame from case *b*, showing the regular structure of the thermo-diffusively unstable

438   cells. Bottom: heat release rate field from the pure H_2 flame from case *a*, where the corrugation

439   results from a hydrodynamic instability with little variation of heat release rate along the flame

440   front.

441

442   **Conclusions**

443   In this paper premixed H_2-CO_2-O_2-N_2 flames with air were investigated first numerically and the findings

444   have been afterwards confirmed in an experimental investigation. The utilization of a validated detailed

445   kinetic mechanism allowed for the evaluation of the effects of initial composition on the laminar burning

446   velocity, the most influential reactions, and the main oxidation paths of the investigated mixtures. The

447   relative contribution of thermal and chemical effects was quantified through the definition of a fictitious

448   CO_2 (FCO_2), acting as an inert species having the same thermal and transport properties as CO_2. The

449   obtained results showed that the presence of CO_2 strongly affects the chemistry of non-carbon

450   containing species because of the modifications in the reaction rate of $CO + OH \leftrightarrows CO_2 + H$, potentially

451   causing significant differences in the ignition behaviour. Further, the effect of CO_2 addition in terms of

452 the flame structure has been investigated with two different numerical setups: the addition of CO_2 leads

453 to a decrease in the mixture's thermal diffusivity and therewith a decrease in the Lewis number. This in

454 turn changes the Markstein number for near-stoichiometric flames from slightly positive values for pure

455 hydrogen flames to negative ones for H_2-CO_2 flames. These results are independent of the employed

456 reaction mechanisms and also if CO_2 is considered an inert species or not. Detailed simulation of a

457 spherically expanding H_2-CO_2 flame shows the expected cellular structures of thermo-diffusively

458 unstable flames, which is not present for the pure hydrogen flame.

459 These results were verified by experiments using a heat flux burner. Adiabatic cellular flames of H_2-CO_2-

460 O_2-N_2 were identified visually and by photographic observations and the cellular structures have been

461 quantified. Under specific experimental conditions, the flames become cellular; this led to significant

462 modification of the flame propagation speed. Increasing the temperature of the burner plate up to

463 T_{plate} = 428 K does not eliminate this instability for H_2-O_2-N_2-CO_2 flames. Lowering the temperature of

464 the burner plate extended the range of equivalence ratios over which cellularity was observed. No direct

465 proportionality between the number of cells and inlet velocity in H_2-O_2-N_2-CO_2 flames was observed.

466 Dependence of the number of cells as a function of equivalence ratio clearly showed a local maximum

467 in the lean mixtures. In future studies, the influence of CO_2/H_2 ratios as well as the influence of pressure

468 and temperature on these instability phenomena will be investigated in more depth.

469

474

475

476 **References**
477 [1] Moulijn JA. Chemical process technology. 2nd ed. Chichester, West Sussex: John Wiley & Sons
478   Inc; 2013.
479 [2] Kroschwitz JI, Kirk RE, Othmer DF, Seidel A (eds.). Kirk-Othmer encyclopedia of chemical
480   technology. 5th ed. Hoboken, NJ: Wiley-Interscience; 2004.
481 [3] García Cortés C, Tzimas E, Peteves SD. Technologies for coal based hydrogen and electricity
482   co-production power plants with CO2 capture. Luxembourg: Office for Official Publications of the
483   European Communities; 2009.
484 [4] Andrews JW. Hydrogen production and carbon sequestration by steam methane reforming and
485   fracking with carbon dioxide. International Journal of Hydrogen Energy 2020;45(16):9279–84.
486   https://doi.org/10.1016/j.ijhydene.2020.01.231.

487   [5]   van Selow ER, Cobden PD, Verbraeken PA, Hufton JR, van den Brink RW. Carbon Capture by
488   Sorption-Enhanced Water−Gas Shift Reaction Process using Hydrotalcite-Based Material. Ind.
489   Eng. Chem. Res. 2009;48(9):4184–93. https://doi.org/10.1021/ie801713a.
490   [6]   Coenen K, Gallucci F, Pio G, Cobden P, van Dijk E, Hensen E et al. On the influence of steam on
491   the CO2 chemisorption capacity of a hydrotalcite-based adsorbent for SEWGS applications.
492   Chem Eng J 2017;314:554–69. https://doi.org/10.1016/j.cej.2016.12.013.
493   [7]   Carboni M, Pio G, Mocellin P, Pilo F, Vianello C, Russo P et al. Experimental and numerical
494   characterization of hydrogen jet fires. International Journal of Hydrogen Energy
495   2022;47(51):21883–96. https://doi.org/10.1016/j.ijhydene.2022.05.010.
496   [8]   Molkov V, Saffers J-B. Hydrogen jet flames. International Journal of Hydrogen Energy
497   2013;38(19):8141–58. https://doi.org/10.1016/j.ijhydene.2012.08.106.
498   [9]   Kim HY, Lee J, Kim NI. Effects of N 2 /CO 2 dilution on flame propagation velocities and
499   quenching distances of oxy-methane premixed mixtures using an Annular-Stepwise-Diverging-
500   Tube (ASDT). Math. Model. Nat. Phenom. 2018;13(6):55.
501   https://doi.org/10.1051/mmnp/2018053.
502   [10] Zhou A, Li X, Ren X, Li X, Gu C. Evaluation of the performance and economy for a hybrid energy
503   storage system using hydrogen and compressed carbon dioxide as the energy carrier. Energy
504   Convers Manag 2022;264:115700. https://doi.org/10.1016/j.enconman.2022.115700.
505   [11] Allam R, Martin S, Forrest B, Fetvedt J, Lu X, Freed D et al. Demonstration of the Allam Cycle:
506   An Update on the Development Status of a High Efficiency Supercritical Carbon Dioxide Power
507   Process Employing Full Carbon Capture. Energy Procedia 2017;114:5948–66.
508   https://doi.org/10.1016/j.egypro.2017.03.1731.
509   [12] Davis SG, Joshi AV, Wang H, Egolfopoulos F. An optimized kinetic model of H2/CO combustion.
510   Proc Combust Inst 2005;30(1):1283–92. https://doi.org/10.1016/j.proci.2004.08.252.
511   [13] Kim YS, Jeon J, Song CH, Kim SJ. Improved prediction model for H2/CO combustion risk using a
512   calculated non-adiabatic flame temperature model. Nucl Eng Technol 2020;52(12):2836–46.
513   https://doi.org/10.1016/j.net.2020.07.040.
514   [14] Miao H, Lu L, Huang Z. Flammability limits of hydrogen-enriched natural gas. International
515   Journal of Hydrogen Energy 2011;36(11):6937–47.
516   https://doi.org/10.1016/j.ijhydene.2011.02.126.
517   [15] Salzano E, Pio G, Ricca A, Palma V. The effect of a hydrogen addition to the premixed flame
518   structure of light alkanes. Fuel 2018;234:1064–70. https://doi.org/10.1016/j.fuel.2018.07.110.
519   [16] Eckart S, Prieler R, Hochenauer C, Krause H. Application and comparison of multiple machine
520   learning techniques for the calculation of laminar burning velocity for hydrogen-methane
521   mixtures. Therm Sci Eng Prog 2022;32:101306. https://doi.org/10.1016/j.tsep.2022.101306.
522   [17] Tan Y, Douglas MA, Thambimuthu KV. CO2 capture using oxygen enhanced combustion
523   strategies for natural gas power plants. Fuel 2002;81(8):1007–16. https://doi.org/10.1016/S0016-
524   2361(02)00014-5.
525   [18] Qian Y, Sun S, Ju D, Shan X, Lu X. Review of the state-of-the-art of biogas combustion
526   mechanisms and applications in internal combustion engines. Renewable Sustainable Energy
527   Rev 2017;69:50–8. https://doi.org/10.1016/j.rser.2016.11.059.
528   [19] Francisco Jr. RW, Costa M, Catapan RC, Oliveira A. Combustion of hydrogen rich gaseous fuels
529   with low calorific value in a porous burner placed in a confined heated environment. Exp Therm
530   Fluid Sci 2013;45:102–9. https://doi.org/10.1016/j.expthermflusci.2012.10.011.
531   [20] Pio G, Ricca A, Palma V, Salzano E. Experimental and numerical evaluation of low-temperature
532   combustion of bio-syngas. International Journal of Hydrogen Energy 2020;45(1):1084–95.
533   https://doi.org/10.1016/j.ijhydene.2019.10.207.
534   [21] Oliveira GP, Sbampato ME, Martins CA, Santos LR, Barreta LG, Boschi Gonçalves RF.
535   Experimental laminar burning velocity of syngas from fixed-bed downdraft biomass gasifiers.
536   Renew Energy 2020;153:1251–60. https://doi.org/10.1016/j.renene.2020.02.083.
537   [22] Djebaili N, Lisbet R, Paillard C, Dupré G. Comparison between the Ignition of H2-Air-CO2 and
538   H2-Air-H2O Mixtures by a Hot Gas Jet. In: Brun R, Dumitrescu LZ, editors. Shock Waves
539   Marseille II: Physico-Chemical Processes and Nonequilibrium Flow. Berlin, Heidelberg: Springer;
540   1995, p. 149–154.
541   [23] Paidi SK, Bhavaraju A, Akram M, Kumar S. Effect of N2/CO2 dilution on laminar burning velocity
542   of H2–air mixtures at high temperatures. International Journal of Hydrogen Energy
543   2013;38(31):13812–21. https://doi.org/10.1016/j.ijhydene.2013.08.024.
544   [24] Eckart S, Pio G, Krause H, Salzano E. Chemical and thermal effects of trace components in
545   hydrogen rich gases on combustion. Chemical Engineering Transactions 2022;90:361–6.
546   https://doi.org/10.3303/CET2290061.

547 [25] Konnov AA, Dyakov IV. Experimental study of adiabatic cellular premixed flames of methane
548   (ethane, propane) + oxygen + carbon dioxide mixtures. Combust Sci Technol 2007;179(4):747–
549   65. https://doi.org/10.1080/00102200601057550.
550 [26] Jin W, Wang J, Yu S, Nie Y, Xie Y, Huang Z. Cellular instabilities of non-adiabatic laminar flat
551   methane/hydrogen oxy-fuel flames highly diluted with CO2. Fuel 2015;143:38–46.
552   https://doi.org/10.1016/j.fuel.2014.11.036.
553 [27] Yu JF, Yu R, Bai XS. Onset of cellular instability in adiabatic H2/O2/N2 premixed flames
554   anchored to a flat-flame heat-flux burner. International Journal of Hydrogen Energy
555   2013;38(34):14866–78. https://doi.org/10.1016/j.ijhydene.2013.09.075.
556 [28] Pio G, Barba D, Palma V, Salzano E. A Numerical Study on the Effect of Temperature and
557   Composition on the Flammability of Methane–Hydrogen Sulfide Mixtures. Combustion Science
558   and Technology 2019;191(9):1541–57. https://doi.org/10.1080/00102202.2018.1564746.
559 [29] Goodwin DG, Speth RL, Moffat HK, Weber BW. Cantera: An object-oriented software toolkit for
560   chemical kinetics, thermodynamics, and transport processes: Version 2.5.1. 2021.
561 [30] Pio G, Palma V, Salzano E. Comparison and Validation of Detailed Kinetic Models for the
562   Oxidation of Light Alkenes. Ind. Eng. Chem. Res. 2018;57(21):7130–5.
563   https://doi.org/10.1021/acs.iecr.8b01377.
564 [31] Battin-Leclerc F. Detailed chemical kinetic models for the low-temperature combustion of
565   hydrocarbons with application to gasoline and diesel fuel surrogates. Prog Energy Combust Sci
566   2008;34(4):440–98. https://doi.org/10.1016/j.pecs.2007.10.002.
567 [32] Pio G, Dong X, Salzano E, Green WH. Automatically generated model for light alkene
568   combustion. Combust Flame 2022;241:112080.
569   https://doi.org/10.1016/j.combustflame.2022.112080.
570 [33] Konnov AA, Mohammad A, Kishore VR, Kim NI, Prathap C, Kumar S. A comprehensive review of
571   measurements and data analysis of laminar burning velocities for various fuel+air mixtures. Prog
572   Energy Combust Sci 2018;68:197–267.
573 [34] Alekseev VA, Konnov AA. Data consistency of the burning velocity measurements using the heat
574   flux method: Hydrogen flames. Combust Flame 2018;194:28–36.
575   https://doi.org/10.1016/j.combustflame.2018.04.011.
576 [35] Pio G, Renda S, Palma V, Salzano E. Safety parameters for oxygen-enriched flames. J Loss
577   Prev Process Ind 2020;65:104151. https://doi.org/10.1016/j.jlp.2020.104151.
578 [36] Damodara VD, Alphones A, Chen DH, Lou HH, Martin C, Li X. Flare performance modeling and
579   set point determination using artificial neural networks. Int J Energy Environ Eng 2020;11(1):91–
580   109. https://doi.org/10.1007/s40095-019-00314-3.
581 [37] Gao X, Yang S, Sun W. A global pathway selection algorithm for the reduction of detailed
582   chemical kinetic mechanisms. Combust Flame 2016;167:238–47.
583   https://doi.org/10.1016/j.combustflame.2016.02.007.
584 [38] Du Wang, Ji C, Wang S, Meng H, Wang Z, Yang J. Further understanding the premixed
585   methane/hydrogen/air combustion by global reaction pathway analysis and sensitivity analysis.
586   Fuel 2020;259:116190. https://doi.org/10.1016/j.fuel.2019.116190.
587 [39] Law CK, Egolfopoulos FN. A kinetic criterion of flammability limits: The C-H-O-inert system.
588   Symp (Int.) Combust 1991;23(1):413–21. https://doi.org/10.1016/S0082-0784(06)80286-9.
589 [40] Kazakov A, Frenklach M. DRM reaction mechanism 1994.
590 [41] Smith GP, Bowman T, Frenklach M, Golden GM, Moriarty N, Eiteneer B et al. GRI-MECH 3.0
591   http://combustion.berkeley.edu/gri-mech/ 2000.
592 [42] Kee RJ, Coltrin ME, Glarborg P. Chemically reacting flow: Theory and practice. Hoboken, NJ:
593   Wiley-Interscience; 2005.
594 [43] Li J, Zhao Z, Kazakov A, Dryer FL. An updated comprehensive kinetic model of hydrogen
595   combustion. Int. J. Chem. Kinet. 2004;36(10):566–75. https://doi.org/10.1002/kin.20026.
596 [44] Konnov AA. Detailed reaction mechanism for small hydrocarbons combustion, Release 0.5.
597   http://homepages.vub.ac.be/~akonnov/ 2000.
598 [45] Ó Conaire M, Curran HJ, Simmie JM, Pitz WJ, Westbrook CK. A comprehensive modeling study
599   of hydrogen oxidation. Int. J. Chem. Kinet. 2004;36(11):603–22.
600   https://doi.org/10.1002/kin.20036.
601 [46] de Goey LPH, van Maaren A, Quax RM. Stabilization of adiabatic premixed laminar flames on a
602   flat flame burner. Combust Sci Technol 1993;92(1-3):201–7.
603 [47] Botha JP, Spalding DB. The Laminar Flame Speed of Propane/Air Mixtures with Heat Extraction
604   from the Flame. Proceedings of the Royal Society A: Mathematical, Physical and Engineering
605   Sciences 1954;225(1160):71–96.
606 [48] van Maaren A, de Goey LPH. Laser doppler thermometry in flat flames. Combust Sci Technol
607   1994;99(1-3):105–18.

608 [49] Eckart S, Pizzuti L, Fritsche C, Krause H. Experimental study and proposed power correlation for
609   laminar burning velocity of hydrogen-diluted methane with respect to pressure and temperature
610   variation. International Journal of Hydrogen Energy 2022(47):6334–48.
611   https://doi.org/10.1016/j.ijhydene.2021.11.243.
612 [50] Döntgen M, Eckart S, Fritsche C, Krause H, Heufer KA. Experimental and chemical kinetic
613   modeling study of trimethoxy methane combustion. Proceedings of the Combustion Institute
614   2022. https://doi.org/10.1016/j.proci.2022.09.023.
615 [51] de Goey LPH, Somers LMT, Bosch WMML, Mallens RMM. Modeling of the Small Scale Structure
616   of Flat Burner-Stabilized Flames. Combust Sci Technol 1995;104(4-6):387–400.
617   https://doi.org/10.1080/00102209508907729.
618 [52] Alekseev VA, Naucler JD, Christensen M, Nilsson EJK, Volkov EN, de Goey LPH et al.
619   Experimental uncertainties of the heat flux method for measuring burning velocities. Combust Sci
620   Technol 2016;188(6):853–94. https://doi.org/10.1080/00102202.2015.1125348.
621 [53] Eckart S, Penke C, Voss S, Krause H. Laminar burning velocities of low calorific and hydrogen
622   containing fuel blends. Energy Procedia 2017(120):149–56.
623   https://doi.org/10.1016/j.egypro.2017.07.148.
624 [54] Shrestha KP, Eckart S, Elbaz AM, Giri BR, Fritsche C, Seidel L et al. A comprehensive kinetic
625   model for dimethyl ether and dimethoxymethane oxidation and NOx interaction utilizing
626   experimental laminar flame speed measurements at elevated pressure and temperature.
627   Combust Flame 2020(218):57–74. https://doi.org/10.1016/j.combustflame.2020.04.016.
628 [55] Eckart S, Cai L, Fritsche C, vom Lehn F, Pitsch H, Krause H. Laminar burning velocities, CO and
629   NOx emissions of premixed polyoxymethylene dimethyl ether flames. Fuel 2021(293).
630 [56] Eckart S, Fritsche C, Krasselt C, Krause H. Determining the laminar burning velocity of nitrogen
631   diluted dimethoxymethane (OME1) using the heat-flux burner method: Numerical and
632   experimental investigations. Int. J. Energy Res. 2020(45):2824–36.
633 [57] Rau F, Hartl S, Voss S, Still M, Hasse C, Trimis D. Laminar burning velocity measurements using
634   the Heat Flux method and numerical predictions of iso-octane/ethanol blends for different preheat
635   temperatures. Fuel 2015;140:10–6.
636 [58] Zhang F, Bonart H, Zirwes T, Habisreuther P, Bockhorn H, Zarzalis N. Direct Numerical
637   Simulation of Chemically Reacting Flows with the Public Domain Code OpenFOAM. In: Kröner D,
638   Resch M, Nagel WE, editors. High Performance Computing in Science and Engineering '14:
639   Transactions of the High Performance Computing Center, Stuttgart (HLRS) 2014. Cham:
640   Springer; 2015, p. 221–236.
641 [59] Zirwes T, Zhang F, Denev JA, Habisreuther P, Bockhorn H. Automated Code Generation for
642   Maximizing Performance of Detailed Chemistry Calculations in OpenFOAM. In: Nagel WE,
643   Kröner D, Resch M, editors. High Performance Computing in Science and Engineering ' 17:
644   Transactions of the High Performance Computing Center, Stuttgart (HLRS) 2017. Cham:
645   Springer; 2018, p. 189–204.
646 [60] Zirwes T, Zhang F, Habisreuther P, Hansinger M, Bockhorn H, Pfitzner M et al. Quasi-DNS
647   Dataset of a Piloted Flame with Inhomogeneous Inlet Conditions. Flow Turbulence Combust
648   2020;104(4):997–1027. https://doi.org/10.1007/s10494-019-00081-5.
649 [61] OpenFOAM. The open surce CFD toolbox.
650 [62] Wen X, Zirwes T, Scholtissek A, Böttler H, Zhang F, Bockhorn H et al. Flame structure analysis
651   and composition space modeling of thermodiffusively unstable premixed hydrogen flames — Part
652   I: Atmospheric pressure. Combust Flame 2022;238:111815.
653   https://doi.org/10.1016/j.combustflame.2021.111815.
654 [63] Zirwes T, Zhang F, Denev JA, Habisreuther P, Bockhorn H, Trimis D. High Performance
655   Computing in Science and Engineering ' 18: Transactions of the High Performance Computing
656   Center, Stuttgart (HLRS) 2018. Springer eBook Collection. Cham: Springer; 2019.
657   https://doi.org/10.1007/978-3-030-13325-2.
658 [64] Zirwes T, Zhang F, Häber T, Bockhorn H. Ignition of combustible mixtures by hot particles at
659   varying relative speeds. Combustion Science and Technology 2019;191(1):178–95.
660   https://doi.org/10.1080/00102202.2018.1435530.
661 [65] Zirwes T, Häber T, Zhang F, Kosaka H, Dreizler A, Steinhausen M et al. Numerical Study of
662   Quenching Distances for Side-Wall Quenching Using Detailed Diffusion and Chemistry. Flow
663   Turbulence Combust 2020. https://doi.org/10.1007/s10494-020-00215-0.
664 [66] Berger L, Kleinheinz K, Attili A, Pitsch H. Characteristic patterns of thermodiffusively unstable
665   premixed lean hydrogen flames. Proc Combust Inst 2019;37(2):1879–86.
666   https://doi.org/10.1016/j.proci.2018.06.072.
667 [67] Wen X, Zirwes T, Scholtissek A, Böttler H, Zhang F, Bockhorn H et al. Flame structure analysis
668   and composition space modeling of thermodiffusively unstable premixed hydrogen flames — Part

669   II: Elevated pressure. Combust Flame 2021:111808.
670   https://doi.org/10.1016/j.combustflame.2021.111808.